

Helical Tendon-Driven Continuum Robot with Programmable Follow-the-Leader Operation

Behnam Moradkhani¹, Raghav Sankaranarayanan¹, Pejman Kheradmand¹, Harshith Jella¹,
Nicholas Ahn², Ajmal Zemmar³ and Yash Chitalia¹

Abstract—Spinal cord stimulation (SCS) is primarily utilized for pain management and has recently demonstrated efficacy in promoting functional recovery in patients with spinal cord injury. Effective stimulation of motor neurons ideally requires the placement of SCS leads in the ventral or lateral epidural space where the corticospinal and rubrospinal motor fibers are located. This poses significant challenges with the current standard of manual steering. In this study, we present a static modeling approach for the *ExoNav*, a steerable robotic tool designed to facilitate precise navigation to the ventral and lateral epidural space. Cosserat rod framework is employed to establish the relationship between tendon actuation forces and the robot's overall shape, and a simulation environment is prepared based on the developed model. The effects of gravity, as an example of an external load, are investigated and implemented in the model and simulation. The experimental results indicate root mean square error (RMSE) values of 1.76 mm, 2.33 mm, 2.18 mm, and 1.33 mm (2.3%, 3.1%, 3.4%, and 2.1% of the robot length) for the tip position estimation across four tested prototypes. Based on the helical shape of the *ExoNav* upon actuation, it is capable of performing follow-the-leader (FTL) motion by adding insertion and rotation DoFs to this robotic system, which is shown in simulation and experimentally. The proposed simulation has the capability to calculate optimum tendon tensions to follow the desired FTL paths while gravity-induced robot deformations are present. Three FTL experimental trials are conducted and the end-effector position showed repeatable alignments with the desired path with maximum RMSE value of 3.75 mm (less than 5% of the robot length). Ultimately, a phantom model demonstration is conducted where the teleoperated robot successfully navigated to the lateral and ventral spinal cord targets. Additionally, the user was able to navigate to the dorsal root ganglia, illustrating *ExoNav*'s potential in both motor function recovery and pain management.

I. INTRODUCTION

Spinal cord stimulation (SCS) is a neuromodulation intervention to treat drug-refractory pain [1]. SCS has also demonstrated versatility in recovery of post spinal cord injury, including the restoration of both voluntary and involuntary functions [2], [3], [4]. Currently, the SCS leads are placed in the dorsal epidural space since this has been

*This work was supported in part by the Kentucky Spinal Cord and Head Injury Research Trust (KSCHIRT) Fund.

¹B. Moradkhani, R. Sankaranarayanan, P. Kheradmand, H. Jella, and Y. Chitalia are with the Healthcare Robotics and Telesurgery Laboratory (Heartlab), University of Louisville, Louisville, KY, USA.

²N. Ahn is with the Department of Orthopedic Surgery, University of Louisville School of Medicine, Louisville, KY, USA.

³A. Zemmar is with the Robley Rex Va Medical Center, Louisville VA Medical Center, Louisville, KY, USA.

Corresponding Author: B. Moradkhani
(b0mora01@louisville.edu)

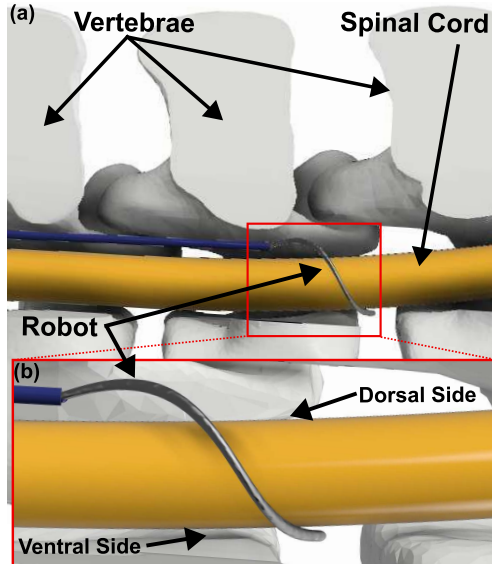


Fig. 1. (a) cross-sectional view of spinal vertebral segments and the spinal cord with *ExoNav* deformed in a helical shape around the spinal cord. (b) Close view of *ExoNav*, navigated from the dorsal spinal cord (entry point) to the ventral spinal cord (target region).

well established for pain treatment. While the pain fibers are located dorsally, motor fibers are located in the ventral and lateral spinal cord. The current standard of manual steering does not permit the surgeon to place the SCS leads in the ventral and lateral epidural space although the benefits and efficacy have been demonstrated [2].

Despite significant advancements in surgical robotics, limited attention has been given to developing robotic solutions specifically for steering SCS leads. While a system [5] has been proposed as a potential solution, it remains a conceptual perspective with no implemented methods or experimental validation. More recently, a hybrid tendon- and magnet-actuated continuum robot [6] was designed to navigate the dorsal spinal cord. However, this system featured a relatively large form factor and lacked evidence of safe navigation in proximity to the delicate spinal structures. In this context, one of the most promising approaches for achieving safe and minimally invasive navigation, particularly relevant to continuum robotics, is the follow-the-leader (FTL) motion.

FTL motion has evolved into a significant research challenge in the field of robotics, receiving heightened attention over the past ten years [7]. This motion strategy entails the device's centerline tracking the path of its leading tip

along a predetermined curved trajectory, thereby minimizing disruption to the surrounding environment. A variety of designs have been developed to achieve FTL motion. These include shape memory alloy (SMA) robots [8], soft inflatable robots [9], [10], concentric tube robots [11], [12], [13], and tendon-driven continuum robots [14], [15], [16]. FTL motion proves especially advantageous in surgical contexts, where navigating delicate anatomical regions, such as the spinal cord, is crucial. Continuum surgical robots enable minimally invasive procedures by accessing complex internal pathways, improving precision in surgeries like laparoscopy and endoscopy, while also reducing patient recovery times and streamlining surgical processes [17], [18]. Consequently, numerous studies have focused on integrating FTL motion into continuum robotic systems to enhance accuracy and minimize risks in sensitive surgical applications.

Geometry-based modeling approaches are commonly employed for tendon-driven continuum robots and catheters due to their ease of derivation, low computational cost, and suitability for real-time applications [19], [20]. However, these methods often rely on simplifying assumptions such as piecewise constant curvature and inextensibility, which introduce significant errors [21], [22], [23]. In surgical settings where precise control and accuracy are critical, such approximations may prove inadequate. As a result, the field is increasingly shifting toward mechanics-based models [24], [25], [26], especially those grounded in Cosserat rod theory [24], which offer a more accurate representation of continuum robot behavior by accounting for axial strain, shear, and tendon-induced effects [27]. With growing computational capabilities, these sophisticated models are becoming viable for surgical applications, enabling higher fidelity in both planning and control.

In this paper we describe the design of a helically notched tendon-driven continuum robot, designed specifically for navigating probes to lateral and ventral spinal cord fiber tracts (Section II). Furthermore, we customize and apply Cosserat rod framework on the proposed robot (Sections II-A and II-B). Upon tendon actuation, the robot bends into an adjustable helical shape. Helical shapes are intentionally chosen since they are naturally capable of performing FTL motions while subjected to appropriate translation and rotation (as investigated in [28]). These translation and rotation inputs, along with appropriate tendon tensions, are optimized for 3D helical FTL operations, based on the developed Cosserat rod model (Sections II-C and II-D). The proposed model and FTL motion accuracies are then evaluated experimentally and a demonstration of the robot performance in a phantom spinal cord model is conducted (Section III). Ultimately, conclusions and future directions are discussed (Section IV).

The main contributions of this manuscript are:

- Customizing the Cosserat rod framework for notched continuum robots, especially with convoluted and complex notch patterns
- Proposing a tendon-tension input optimization method for close-to-FTL operation under external loads (e.g. gravity)

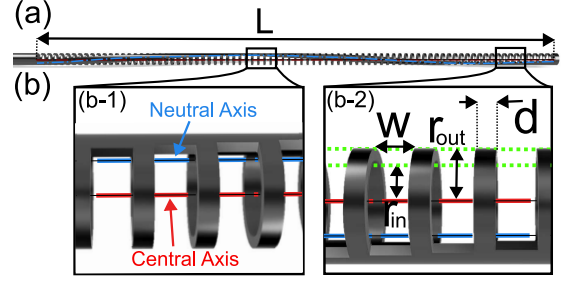


Fig. 2. (a) Structure of *ExoNav*: a nitinol tube with helically machined rectangular notches along its length. Straight central axis and helical neutral axis are depicted over the structure. (b) Zoomed-in views showing the (a) central and neutral axis locations, and (b) notch patterns and their dimensions.

- Conducting a lateral and ventral navigation inside a phantom spinal cord model

II. DESIGN AND MODEL

The *ExoNav* is a micromachined nitinol tube robot designed for the precise placement of SCS electrodes within the lateral and ventral epidural space. The structural design of the robot incorporates helical unidirectional asymmetric notches [29] on a hollow nitinol tube with inner and outer radii of r_{in} and r_{out} , respectively. Each notch has an edge of width w parallel to the tube's central axis and is separated by a segment of length d in the same direction (see Fig. 2). The orientation of these notches is configured such that the pattern completes a full rotation around the tube's circumference over its total length L (see Fig. 2(a)). A nitinol actuation tendon with a radius of r_t , routed inside the tube and anchored at its tip, is capable of deforming the robot into a helical shape (see Fig. 3(a)). The notched tube is then placed inside an enclosing outer tube which can constrain some proximal portion of the robot, depending on how much of the robot is exposed out of the outer tube. Four different prototypes are manufactured based on this design description. Prototypes 1 and 2 share identical dimensions ($r_{in} = 0.457$ mm, $r_{out} = 0.572$ mm, $w = 0.4$ mm, $d = 0.2$ mm, $L = 75.4$ mm, and $r_t = 0.05$ mm), differing only in the value of ψ (determining the depth of the notches, hence the overall compliance of the prototype, see Fig. 3(b)), which is 90° for prototype 1 and 107° for prototype 2. Similarly, prototypes 3 and 4 have the same geometric parameters ($r_{in} = 0.851$ mm, $r_{out} = 0.953$ mm, $w = 0.5$ mm, $d = 0.3$ mm, $L = 63.27$ mm, and $r_t = 0.1$ mm), with ψ set to 90° for prototype 3 and 126° for prototype 4.

A. Static Equilibrium Equations for Tendon-Driven Robots

Our proposed model is based on the customized general Cosserat rod theory for tendon-driven continuum robots [24]. All the kinematic parameters and mechanical properties, varying over the robot length, are defined as functions of the arc-length s , and d/ds is denoted by the dot (‘) notation.

$$\dot{\mathbf{p}} = \mathbf{R}\mathbf{v} \quad (1)$$

$$\dot{\mathbf{R}} = \mathbf{R}\hat{\mathbf{u}} \quad (2)$$

$\mathbf{p} \in \mathbb{R}^3$ is the position vector of the robot neutral axis defined in the global frame (see Fig. 3(a)) and $\mathbf{R} \in SO(3)$ describes the robot body material orientation. Kinematic parameters \mathbf{v} and \mathbf{u} describe geometric rates of change in linear and angular directions according to the local frame at s (in Fig. 3(b), ‘x’ and ‘y’ are specifying the local coordinate system at s). Furthermore, the hat ($\hat{\cdot}$) operator maps a vector in \mathbb{R}^3 to a skew-symmetric matrix in $SO(3)$ such that the cross product of two vectors can be represented as a matrix-vector multiplication. To complete the model equations, the balance of linear momentum and angular momentum of the continuum robot is formulated as:

$$\begin{bmatrix} \dot{\mathbf{v}} \\ \dot{\mathbf{u}} \end{bmatrix} = \begin{bmatrix} \mathbf{K}_{\text{se}} + \mathbf{K}_{11} & \mathbf{K}_{12} \\ \mathbf{K}_{21} & \mathbf{K}_{\text{bt}} + \mathbf{K}_{22} \end{bmatrix}^{-1} \begin{bmatrix} \mathbf{a} \\ \mathbf{b} \end{bmatrix} \quad (3)$$

Stiffness matrix for shear and extension is denoted as $\mathbf{K}_{\text{se}} = \text{diag}(GA, GA, EA)$, and similarly for bending and twist, $\mathbf{K}_{\text{bt}} = \text{diag}(EI_x, EI_y, EI_z)$ is used. E is the elastic modulus, commonly put equal to 75GPa for nitinol, and similarly, G is the shear modulus, commonly put equal to 25GPa for nitinol. A is the robot cross-section area, and I_e is the second moment of area in the direction of $e \in \{x, y, z\}$, all of which are assumed to be constant over s . Furthermore, $\mathbf{K}_{11} = -\tau(\hat{\mathbf{p}}_t^b)^2/||\mathbf{p}_t^b||^3$, where τ is the applied tension to the actuation tendon, $\mathbf{r} = [r_x, r_y, 0]^T$ is the local representation of the tendon path, and $\hat{\mathbf{p}}_t^b = \hat{\mathbf{u}}\mathbf{r} + \dot{\mathbf{r}} + \mathbf{v}$ is the tendon path unit tangent vector defined in the local frame. With \mathbf{K}_{11} obtained, $\mathbf{K}_{12} = -\mathbf{K}_{11}\hat{\mathbf{r}}$, $\mathbf{K}_{21} = \hat{\mathbf{r}}\mathbf{K}_{11}$, and $\mathbf{K}_{22} = -\hat{\mathbf{r}}\mathbf{K}_{11}\hat{\mathbf{r}}$ are calculated consequently. Ultimately, the elements of the vector on the right-hand side of Eq. (3) are defined.

$$\mathbf{a} = \mathbf{K}_{\text{se}}\dot{\mathbf{v}}^* - \hat{\mathbf{u}}\mathbf{K}_{\text{se}}(\mathbf{v} - \mathbf{v}^*) - \mathbf{R}^T\mathbf{f}_e - \mathbf{K}_{11}(\hat{\mathbf{u}}\hat{\mathbf{p}}_t^b + \hat{\mathbf{u}}\dot{\mathbf{r}} + \ddot{\mathbf{r}}) \quad (4)$$

$$\mathbf{b} = \mathbf{K}_{\text{bt}}\dot{\mathbf{u}}^* - \hat{\mathbf{u}}\mathbf{K}_{\text{bt}}(\mathbf{u} - \mathbf{u}^*) - \hat{\mathbf{u}}\mathbf{K}_{\text{se}}(\mathbf{v} - \mathbf{v}^*) - \mathbf{R}^T\mathbf{l}_e - \hat{\mathbf{r}}\mathbf{K}_{11}(\hat{\mathbf{u}}\hat{\mathbf{p}}_t^b + \hat{\mathbf{u}}\dot{\mathbf{r}} + \ddot{\mathbf{r}}) \quad (5)$$

The asterisk (*) notation indicates robot configuration when no tendon tension is applied. Additionally, \mathbf{f}_e and \mathbf{l}_e are the applied external distributed forces (e.g. gravity) and moments respectively.

B. Specific Static Equilibrium Equations for the ExoNav

To apply the Cosserat rod model to micromachined tube robots, we define the “effective area” (denoted by A) of the structure, which serves as the robot’s backbone. In this context, the “effective area” refers to the unnotched, continuous longitudinal segment of the tube that appears as a circular arc, spanning the angle ψ around the center, in each cross-section of the robot (see Fig. 3(b)). Accordingly, $\mathbf{p}(s)$ is defined pointed to the neutral axis of this “effective area” along the robot (see Fig. 3(b)). The rest of the circular cross-section of the tube can be ignored, since its sole purpose is to secure the actuation tendon inside the tube, not playing a role in robot deformations (as long as the edges of the neighboring notches do not contact due to high deformations).

$$A = \frac{\psi(r_{\text{out}}^2 - r_{\text{in}}^2)}{2} \quad (6)$$

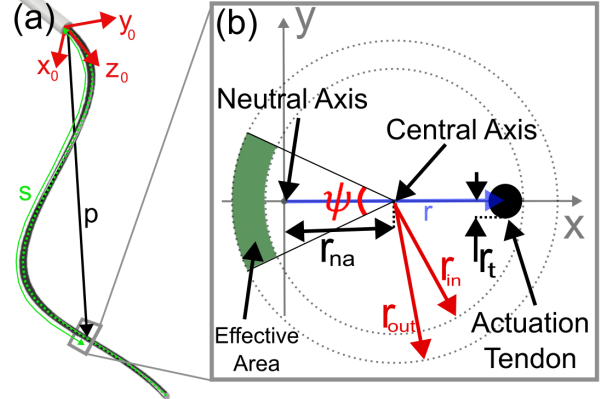


Fig. 3. (a) The *ExoNav* bending into a helical curve, with the global coordinate frame defined at the robot base. The position vector $\mathbf{p}(s)$ denotes the neutral axis at an arbitrary arc-length s . (b) Cross-sectional view at arc-length s , showing the locations of the actuation tendon, the neutral axis, and the effective cross-sectional area in the local coordinate frame.

To define \mathbf{p} , note that the neutral axis is deviated from the central axis by $r_{na} = |(\int x dA)/A|$ (See Fig. 3(b)).

$$r_{na} = \frac{4 \sin(\psi/2)(r_{\text{out}}^3 - r_{\text{in}}^3)}{3 \psi(r_{\text{out}}^2 - r_{\text{in}}^2)} \quad (7)$$

Based on the direction of this deviation and the local coordinate frames origin on the deviated neutral axis, we define the material orientation matrix \mathbf{R} such that the x-axis of the local coordinate frame always points towards the central axis and away from the effective area (see Fig. 3(b)). This specific definition of \mathbf{R} results in cross-sectional inertia being independent of s , hence the local parameters at each cross section (such as second moments of area, location of the neutral axis, and location of the actuation tendon) are invariant with s . Furthermore, the second moment of area in x-y directions (see Fig. 3(b)) are obtainable at the robot’s neutral axis via the parallel axis theorem (similar approach used in [14]).

$$I_x = \frac{(\psi + \sin(\psi))(r_{\text{out}}^4 - r_{\text{in}}^4)}{8} \quad (8)$$

$$I_y = \frac{(\psi - \sin(\psi))(r_{\text{out}}^4 - r_{\text{in}}^4)}{8} - Ar_{na}^2 \quad (9)$$

And subsequently, $I_z = I_x + I_y$. Generally, the actuation tendon tends to take the shortest path possible as it is subjected to tension, and in the case of micromachined tubes, if the actuation tendon is not constrained to a specific path, it always occupies a position diametrically opposite to the “effective area” (see Fig. 3(b)). Therefore, the local tendon path is calculated as $\mathbf{r} = [r_{na} + r_{in} - r_t, 0, 0]^T$. The local coordinates at $s = 0$ (robot base) are defined to align with the global coordinates (see Fig. 3(a)).

$$\mathbf{p}^* = \begin{bmatrix} -r_{na}\cos(2\pi s/L_{na}) \\ -r_{na}\sin(2\pi s/L_{na}) \\ Ls/L_{na} \end{bmatrix} \quad (10)$$

$$\mathbf{R}^* = \begin{bmatrix} \cos(2\pi s/L_{na}) & -\sin(2\pi s/L_{na}) & 0 \\ \sin(2\pi s/L_{na}) & \cos(2\pi s/L_{na}) & 0 \\ 0 & 0 & 1 \end{bmatrix} \quad (11)$$

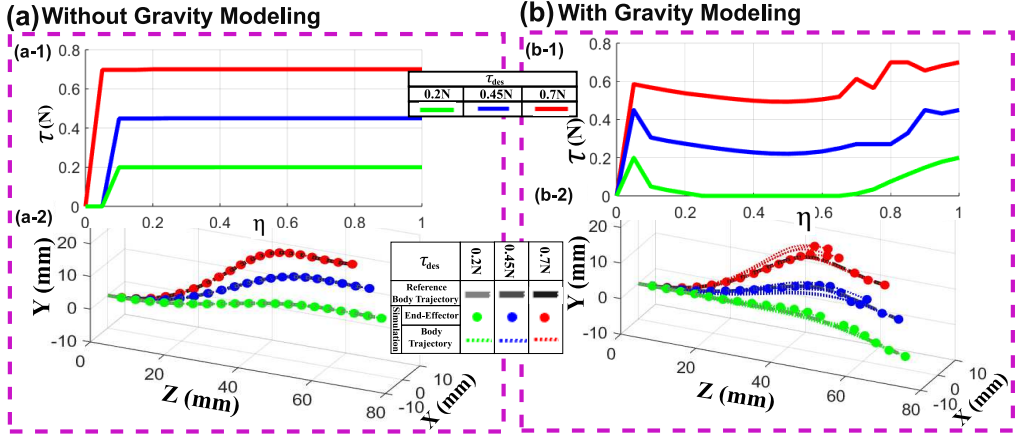


Fig. 4. (a) ExoNav simulation results without gravity modeling: (a-1) optimized τ values along different FTL trajectories and (a-2) simulated ExoNav end-effector and body trajectories evolution compared to the reference FTL trajectory. (b) ExoNav simulation results with gravity effects included: (b-1) optimized τ values along different FTL trajectories and (b-2) simulated ExoNav end-effector and body trajectories evolution compared to the reference FTL trajectory.

The length of the neutral axis is denoted by $L_{na} = \sqrt{L^2 + (2\pi r_{na})^2}$. Substituting \mathbf{p}^* and \mathbf{R}^* in Eqs. (1) and (2), \mathbf{v}^* and \mathbf{u}^* are obtained.

$$\mathbf{v}^* = [0, -2\pi r_{na}/L_{na}, L/L_{na}]^T \quad (12)$$

$$\mathbf{u}^* = [0, 0, 2\pi/L_{na}]^T \quad (13)$$

By substituting these specific parameters in Eqs. (1), (2), and (3), the overall model equations are obtained. For state variables \mathbf{p} and \mathbf{R} in the model equations, initial conditions are obtained by substituting $s = 0$ in Eqs. (10) and (11). Furthermore, tendon termination boundary conditions are defined for the kinematic state variables \mathbf{v} and \mathbf{u} .

$$\mathbf{v}(L_{na}) = \mathbf{v}^*(L_{na}) - \mathbf{K}_{se}^{-1}(\tau \frac{\dot{\mathbf{p}}_t^b(L_{na})}{\|\dot{\mathbf{p}}_t^b(L_{na})\|}) \quad (14)$$

$$\mathbf{u}(L_{na}) = \mathbf{u}^*(L_{na}) - \mathbf{K}_{bt}^{-1}\hat{\mathbf{r}}(L_{na})(\tau \frac{\dot{\mathbf{p}}_t^b(L_{na})}{\|\dot{\mathbf{p}}_t^b(L_{na})\|}) \quad (15)$$

where actuation tendon tension is denoted as τ and treated as the input of the model. The model equations are implemented in MATLAB and solved using a shooting method.

C. Progressive and FTL Motion Simulation

We define “progressive motion” as a kinematic behavior primarily characterized by translational movement along the robot’s longitudinal axis, which may be accompanied by rotation. Let L_p denote the exposed length of the robot extending beyond an enclosing outer tube. To quantify the extent of this motion, we introduce the “progression factor” $\eta \in [0, 1]$, where $\eta = 0$ corresponds to the robot being fully retracted within the outer tube, and $\eta = 1$ represents the robot being fully extended out.

$$L_p = \eta L \quad (16)$$

Note that a necessary condition for classifying a motion as “progressive motion” is a change in the progression factor

η (either increasing or decreasing). Within this context, the arc-length parameter in “progressive motion” is defined as $s_p \in [0, \eta L_{na}]$ (focused only on the exposed length of the robot). Furthermore, the tip of the outer tube is designated as the robot base, as it marks the onset of deformation along the robot body. Consequently, the initial values $\mathbf{p}(0)$ and $\mathbf{R}(0)$ are redefined by substituting $s = (1 - \eta)L_{na}$ into Eqs. (10) and (11), thereby accounting for the new base location.

A helical deformable structure is naturally capable of performing FTL motion upon a simultaneous rotation and translation (related through the pitch of the helix, which is $\frac{L}{2\pi}$ for the case of the ExoNav) as it comes out of a rigid outer tube. In this regard, the FTL motion is a subset of the general “progressive motion”. In our case, the FTL motion requirement depends on the applied rotation ($\phi_p = 2\pi(\eta - 1)$) and tendon tension (τ) along the progressive motion. A “progressive motion” simulation is utilized based on the developed Cosserat rod statics model, to obtain the appropriate tendon tension input.

To initiate the simulation, first the model is solved with η set to 1 and τ set to an arbitrary desired value (τ_{des}). The resulted robot body trajectory determines the FTL reference trajectory, meaning that throughout the FTL motion, the exposed robot body trajectory and end-effector need to closely align with this FTL reference trajectory. After obtaining the FTL reference trajectory, we run the simulation iteratively and increase η from 0 to 1 with a certain step size ($\Delta\eta$). In each iteration, η is kept constant, while the model is solved for different τ values and the resulted shapes are compared to the FTL reference trajectory until the exposed robot body trajectory is inside an acceptable proximity from the reference trajectory. In this simulation, L_p and ϕ_p are substituted in the model equations to satisfy the FTL motion requirements. We executed this simulation with different τ_{des} values (0.2N, 0.45N, and 0.7N) and $\Delta\eta = 0.05$, and the obtained τ values throughout the progressive motion turned out as constant values (See Fig. 4(a-1)). The simulated

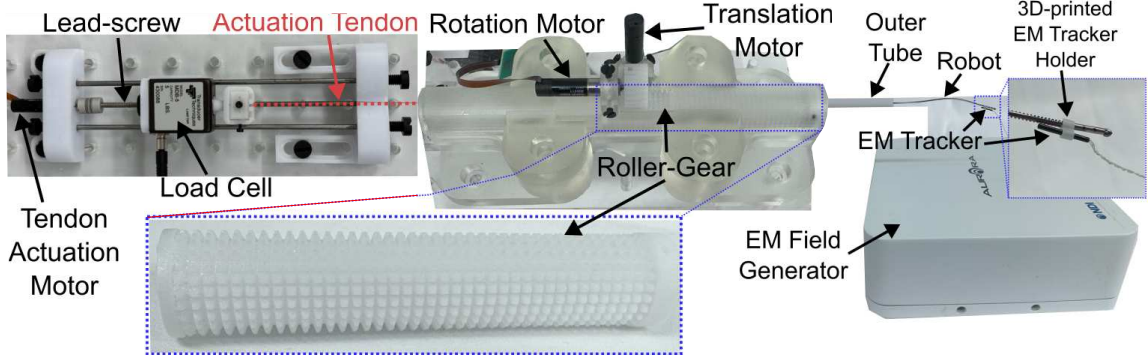


Fig. 5. Components of the actuation setup, with the tendon pulling mechanism on the left, the dual-DoF roller-gear mechanism in the center (inset shows circumferential and longitudinal gear heads), and the robot protruding from the outer tube on the right. An EM tracker is attached to the robot via a 3D-printed holder (inset on the right), with the EM field generator positioned beneath the exposed robot.

robot end-effector and body trajectories for each simulation show close alignment with the FTL reference trajectory (See Fig. 4(a-2)). These results show that for performing a FTL navigation using ExoNav, we just need to control the actuation tendon tensions to keep it constant as the robot is being translated and rotated out of the outer tube. Note that for smaller τ_{des} , the optimized τ in the first iteration(s) might stay at 0 N. The reason is that the robot is barely extended out of the outer tube and the straight body trajectory is already close to the FTL reference trajectory, therefore the simulation stops at the initial τ in searching for the best τ (See graphs for $\tau_{des} = 0.2N$ and $0.45N$ in Fig. 4(a-1)). Note that the aforementioned simulation assumes lack of external forces. However, external forces (especially gravity) can potentially cause the robot shape to deviate from a perfect helix. In this scenario, the developed FTL motion simulation is programmed to obtain the most optimal tendon forces that keep the robot body trajectory at minimum distance from the reference FTL motion trajectory.

D. Gravity Effect Modeling

The exerted gravity force to the robot can be calculated and inserted into the model as a uniformly distributed external force (\mathbf{f}_e in Eq. 4). To do so, the mass density of nitinol ($\rho = 6255 \text{ Kg/m}^3$) is utilized to calculate the linear mass density (λ) of ExoNav, considering the notches along the robot:

$$\lambda = \frac{(\pi d + \psi w/2)(r_{out}^2 - r_{in}^2)}{d + w} \rho \quad (17)$$

Assuming the gravity force being towards $-X_0$ (according to the depicted global frame in Fig. 3(a)), the external gravitational force can be calculated as:

$$\mathbf{f}_e = \lambda g [-1, 0, 0]^T \quad (18)$$

where $g = 9.81 \text{ m/s}^2$ is the gravitational acceleration.

This external force is implemented in the simulation and model equations, and a similar simulation instruction (as described in subsection II-C) is followed. The optimized τ for each simulation with a specific τ_{des} seem completely different from the prior results where no gravity effect was modeled. In the first iterations, τ increases to a certain

value commonly lower than its corresponding τ_{des} , which then follows a slight U-shaped curve, and in final iterations, optimized τ values seem to converge to τ_{des} (See Fig. 4(b-1)). FTL reference trajectories and simulated robot body trajectories show significant bending towards $-X_0$ (gravitational force direction) compared to the case with no gravity modeling (See Fig. 4(a-2) and (b-2)). The robot body trajectories and end-effector along the simulated progressive motion are kept at a close distance from the FTL reference trajectory, with a few observable deviations, especially towards the end of the progressive motion (See Fig. 4(b-2)). These deviations appear as some jaggedness in the optimized τ values (See Fig. 4(b-1)). These deviations and jaggedness are most probably due to relatively high error margins or multiple local minima in the search span of the simulation program. There are several ways to resolve these issues to have closer alignments with the FTL reference trajectory and subsequently, smoother optimized τ values over η variations, which are potential focuses for future studies.

III. EXPERIMENTAL RESULTS

A. Experimental Setup

The experimental setup consists of a motorized lead-screw mechanism capable of linearly translating a 3D-printed bracket, which holds a load-cell (MDB-5, Transducer Techniques) to measure tendon tensions (see Fig. 5). Additionally, to provide translation and rotation DoFs, we used a 3D-printed motorized roller-gear mechanism [30], capable of simultaneous rotation and translation using two individual motors implemented perpendicularly. We also used 3D-printed outer tubes customized for each prototype (see Fig. 5). We utilized a 6-DoF electromagnetic (EM) tracking system (NDI Aurora, Northern Digital Inc, Waterloo, Ontario, Canada) to measure the position of different points on the robot. EM tracking system consists of two main parts: EM field generator and a small tracking module, called the EM tracker. We designed and 3D-printed small holder components that provides connection between the EM tracker and the robot body (see Fig. 5). The offset between the EM tracker and the robot body is measured and compensated, hence all the provided results are denoting the measured points on

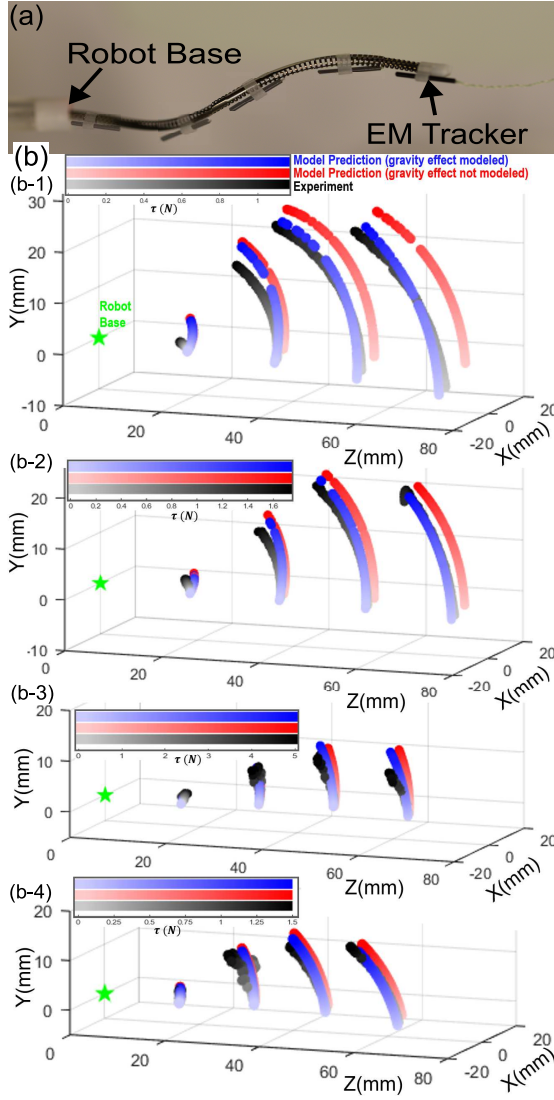


Fig. 6. (a) Robot fully extended from the outer tube and bent into a helical shape, with the EM tracker placed at four distinct locations along its length and at the base. (b) Comparison of experimental position measurements with model predictions, with and without gravity modeling, for (b-1) prototype 1, (b-2) prototype 2, (b-3) prototype 3, and (b-4) prototype 4.

the robot body. Three DC motors (RE 8 Ø8 mm, Precious Metal Brushes, 0.5 Watt, with terminals, Maxon international ltd., Switzerland) are used in tendon pulling and roller-gear mechanisms, all of which are controlled by a Texas Instrument LAUNCHXL-F28379D LaunchPad, utilized for motor control and to gather force and motor encoder data in the MATLAB/Simulink environment. Furthermore, we gathered the synchronized position data from EM tracking system in MATLAB.

B. Model Validation Experiment

Conducting experimental trials on each prototype, first, the EM tracker is placed at the robot's base to set the origin of the global frame. Then the EM tracker is placed at locations closely corresponding to arc-length values of $s = 0.25L_{na}$, $s = 0.5L_{na}$, $s = 0.75L_{na}$, and $s = L_{na}$, and the robot is

TABLE I
PREDICTION ERRORS WITH AND WITHOUT MODELING GRAVITY.

Prototype	s	Gravity		Not Modeled		Modeled	
		MED (mm)	RMSE (mm)	MED (mm)	RMSE (mm)	MED (mm)	RMSE (mm)
1	$0.25L_{na}$	4.11	1.67	6.08	2.48		
	$0.50L_{na}$	2.37	1.43	4.60	1.90		
	$0.75L_{na}$	3.30	2.16	2.88	1.40		
	$1.00L_{na}$	7.71	4.18	4.32	1.76		
2	$0.25L_{na}$	1.73	0.87	2.92	1.18		
	$0.50L_{na}$	2.18	1.51	3.06	1.19		
	$0.75L_{na}$	3.51	2.69	2.68	1.22		
	$1.00L_{na}$	6.93	3.30	5.03	2.33		
3	$0.25L_{na}$	3.46	3.15	1.13	0.44		
	$0.50L_{na}$	9.28	5.67	2.30	0.76		
	$0.75L_{na}$	8.08	6.95	3.47	1.41		
	$1.00L_{na}$	11.03	9.60	5.76	2.18		
4	$0.25L_{na}$	3.36	2.81	0.52	0.26		
	$0.50L_{na}$	4.20	3.09	3.75	1.63		
	$0.75L_{na}$	4.40	3.61	2.29	1.29		
	$1.00L_{na}$	6.92	5.61	2.43	1.33		

actuated in each case (see Fig. 6(a)). Similar experiments are conducted across different prototypes, and τ values as well as EM position data are recorded. The gathered τ values are then fed into the developed model to predict ExoNav's deformations with and without gravity modeling (See Fig. 6(b)). The model prediction results show close alignment between the experiment data and the gravity-included model predictions, while model predictions without including gravity are deviated (especially in more flexible prototypes, e.g. prototype 1 shown in Fig. 6(b-1)) from the experiment data, emphasizing the significant effect of external forces on the resulted robot deformation and the necessity to model these external loads. In addition to the obtained graphs (in Fig. 6(b)), corresponding maximum Euclidean distance (MED) errors and root mean square errors (RMSE) are reported for predictions with and without modeling gravity (see Table I). These results show that, overall, including gravity effects in the model reduces the MED and RMSE values which become more observable in measured points closer to the robot end-effector.

C. Tendon Tension Control and FTL Motion Experiment

To perform an arbitrary “progressive motion”, three input commands, including rotation, translation, and tendon tension, must be applied to the experimental setup. However, for

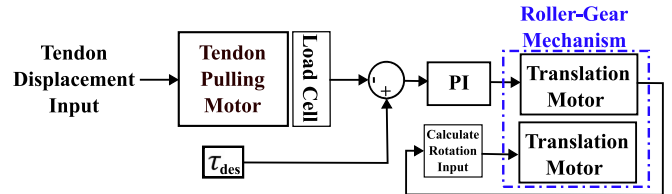


Fig. 7. Schematic of the tendon tension control system implemented during the FTL motion experiment.

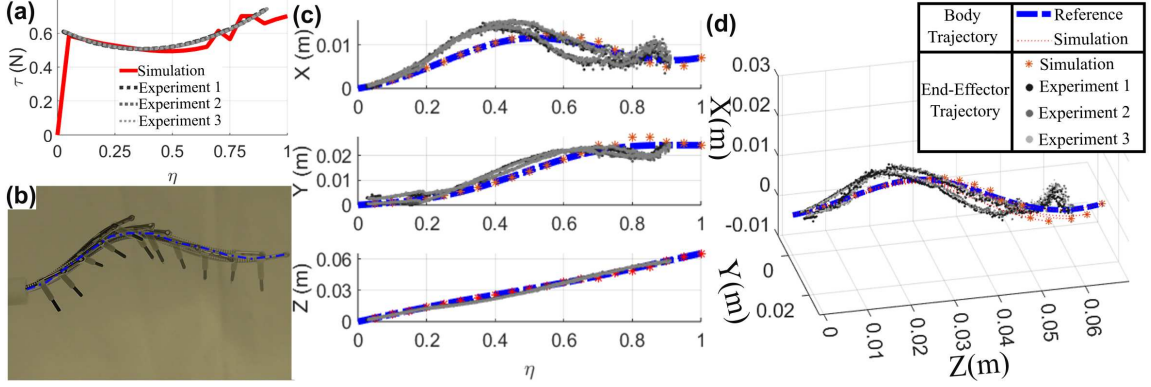


Fig. 8. (a) Simulated and experimental tendon tensions plotted as a function of the progression factor during FTL motion. (b) Robot body motion in the FTL experiment closely follows the reference FTL trajectory. (c) End-effector position plotted as a function of progression factor in simulation and experiments compared to the reference trajectory. (d) 3D visualization of end-effector positions from simulation and experiments alongside the reference FTL trajectory.

FTL motion, rotation and translation inputs are obtained in a dependent fashion, based on η . Therefore, a feedback control system with a PI controller is implemented in Simulink and connected to the utilized micro-controller board. Considering the low speed of the tendon pulling mechanism compared to the motors of the roller-gear mechanism, the controller is implemented on the DoFs that the roller-gear mechanism provides, limiting the overall actuation velocity to the motor of the tendon pulling mechanism, hence applying η indirectly. In this tendon tension control system, we apply a tendon displacement value to the tendon pulling mechanism, which causes the tendon tension to change, followed by the roller-gear translation motor actuation based on the PI controller output, so that the tendon tension gets adjusted. Based on the applied translation, η is calculated, and the appropriate rotation is obtained consequently, and is applied to the rotation motor of the roller-gear mechanism (see Fig. 7). We iteratively tested and finally adjusted the PI controller proportional and integral gains as $k_P = k_I = 50$.

As observed in subsection II-D, the gravity-induced deformations make the FTL reference trajectory deviate to a distorted helix which requires a non-constant τ along η to keep ExoNav close to the corresponding FTL reference trajectory. To avoid sudden changes in the actuation mechanism due to jaggedness observed in τ signals (See Fig. 4(b-1)), a second-order polynomial is fitted (using MATLAB curve fitting toolbox) to the optimized τ signal for $\tau_{des} = 0.7N$ (see Fig. 8(a)). The second-order polynomial curve, $\tau_{FTL}(\eta) = 0.6492\eta^2 - 0.5159\eta + 0.6088$, is utilized to conduct three trials of FTL motion experiment using prototype 1.

The EM tracking module is placed at the tip of the robot to gather end-effector position data (see Fig. 8(b)). The obtained data from both simulation and all three experiments are compared to the FTL reference trajectory (see Fig. 8(c) and (d)). The simulation results show close alignment with the reference trajectory and an RMSE value of 1.0706 mm. The experiment results show RMSE values of 3.6433 mm, 3.6288 mm, and 3.7481 mm for experiment trials 1 to 3, respectively. Comparison between different experiment trials

shows a consistent and repeatable behavior. End-effector position errors in these experimental trials are primarily due frictions (between the outer tube inner walls and the robot), EM tracking module assembly weight, and tendon tension polynomial approximation errors.

D. Robot Demonstration in Phantom Spinal Cord Model

To demonstrate ExoNav's ability to reach clinically relevant anatomical targets, we conducted a set of navigation experiments inside a spinal cord phantom model which includes a 3D-printed mock spinal cord placed inside the 3D-printed spinal canal. The robot was inserted through the dorsal entry and a joystick was used to provide teleoperation for the operator, controlling translation, rotation, and tendon actuation via dedicated joystick key pairs. The operator successfully navigated to the lateral and then ventral target areas with great precision (See Fig. 9(a)). The navigation process consisted of iterative translations and tendon actuation, which was then accompanied by corrective rotations to adjust the helical shape of ExoNav to reach the targets. The user also attempted to navigate to the dorsal root ganglia (DRG) regions and successfully navigated to these additional targets (See Fig. 9(b)). Navigating to the DRGs is a promising capability for pain management applications which was not considered as a primary goal of ExoNav design, but it was found capable to achieve it. Overall, the user was able to navigate around the spinal cord with ease, avoiding unnecessary maneuvers

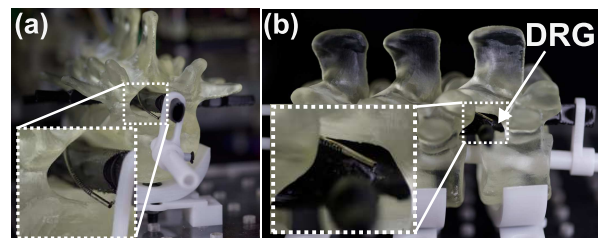


Fig. 9. ExoNav navigation to the (a) ventral spinal cord and (b) DRG region inside a spinal cord phantom model.

that are common with manual SCS navigation techniques. Although ExoNav is manually controlled in these demonstrations, the observed paths are qualitatively consistent with the proposed model and FTL motion paths. ExoNav does not include an SCS electrode integration mechanism and exploring possible latching mechanisms for this purpose is one of the future horizons for this research line.

IV. CONCLUSION

In this manuscript, we described the design of ExoNav, a notched-tube continuum robot with convoluted notch patterns to acquire helical paths to reach lateral and ventral spinal cord fibers to implement SCS electrodes in proximity to the motor tracts. We customized Cosserat rod model equations for tendon-driven continuum robots to include the convoluted notch design and implemented a simulation environment to validate the developed model and analyze ExoNav's capability to execute FTL motion. The effect of gravity as an example of a possible external force is investigated and implemented in the developed model. We also validated our model and tested ExoNav FTL operation experimentally, using an actuation tendon tension PI control system. Ultimately, we show ExoNav capability in maneuvering to the lateral and ventral spinal cord tracts, as well as the DRG of a phantom spinal cord model. Future direction include integration of the actual SCS electrode on the robot and further developing the tendon tension optimization program for real-time applications.

REFERENCES

- [1] J. Taylor, R. Reddy, S. Yin, C. Cui, M. Huang, C. Huang, R. Rao, D. G. Baker, A. Simmons, D. Souza *et al.*, “Spinal cord stimulation in chronic pain: evidence and theory for mechanisms of action,” *Bioelectronic medicine*, vol. 5, pp. 1–41, 2019.
- [2] A. K. Afridi, A. G. Steele, C. Martin, D. G. Sayenko, and S. M. Barber, “Ventral epidural stimulation for motor recovery after spinal cord injury: illustrative case,” *Journal of Neurosurgery: Case Lessons*, vol. 8, no. 12, 2024.
- [3] D. Darrow, D. Balser, T. I. Netoff, A. Krassioukov, A. Phillips, A. Parr, and U. Samadani, “Epidural spinal cord stimulation facilitates immediate restoration of dormant motor and autonomic supraspinal pathways after chronic neurologically complete spinal cord injury,” *Journal of neurotrauma*, vol. 36, no. 15, pp. 2325–2336, 2019.
- [4] M. L. Gill, P. J. Grahn, J. S. Calvert, M. B. Linde, I. A. Lavrov, J. A. Strommen, L. A. Beck, D. G. Sayenko, M. G. Van Straaten, D. I. Drubach *et al.*, “Neuromodulation of lumbosacral spinal networks enables independent stepping after complete paraplegia,” *Nature medicine*, vol. 24, no. 11, pp. 1677–1682, 2018.
- [5] H. Torlakcik, C. Sarica, P. Bayer, K. Yamamoto, C. Iorio-Morin, M. Hodaie, S. K. Kalia, J. S. Neimat, J. Hernesniemi, A. Bhatia *et al.*, “Magnetically guided catheters, micro-and nanorobots for spinal cord stimulation,” *Frontiers in Neurorobotics*, vol. 15, p. 749024, 2021.
- [6] H. Jella, B. Moradkhani, P. Kheradmand, A. Zemmar, and Y. Chitalia, “Exonav: A novel robotic steering and latching mechanism for spinal cord stimulation electrodes,” *IEEE/ASME Transactions on Mechatronics*, 2024.
- [7] C. Culmone, F. S. Yikilmaz, F. Trauzettel, and P. Breedveld, “Follow-the-leader mechanisms in medical devices: a review on scientific and patent literature,” *IEEE Reviews in Biomedical Engineering*, vol. 16, pp. 439–455, 2021.
- [8] D. Palmer, S. Cobos-Guzman, and D. Axinte, “Real-time method for tip following navigation of continuum snake arm robots,” *Robotics and Autonomous Systems*, vol. 62, no. 10, pp. 1478–1485, 2014.
- [9] E. W. Hawkes, L. H. Blumenschein, J. D. Greer, and A. M. Okamura, “A soft robot that navigates its environment through growth,” *Science Robotics*, vol. 2, no. 8, p. eaan3028, 2017.
- [10] M. M. Coad, R. P. Thomasson, L. H. Blumenschein, N. S. Usevitch, E. W. Hawkes, and A. M. Okamura, “Retraction of soft growing robots without buckling,” *IEEE Robotics and Automation Letters*, vol. 5, no. 2, pp. 2115–2122, 2020.
- [11] H. B. Gilbert, J. Neimat, and R. J. Webster, “Concentric tube robots as steerable needles: Achieving follow-the-leader deployment,” *IEEE Transactions on Robotics*, vol. 31, no. 2, pp. 246–258, 2015.
- [12] A. Garriga-Casanovas and F. Rodriguez y Baena, “Complete follow-the-leader kinematics using concentric tube robots,” *The International Journal of Robotics Research*, vol. 37, no. 1, pp. 197–222, 2018.
- [13] L. Xie, L. Zhu, X. Jin, and A. Song, “Curvature-based continuous steering of stiffness-dominant concentric tube robots,” *IEEE Transactions on Automation Science and Engineering*, 2025.
- [14] S. Jeong, Y. Chitalia, and J. P. Desai, “Design, modeling, and control of a coaxially aligned steerable (coast) guidewire robot,” *IEEE Robotics and Automation Letters*, vol. 5, no. 3, pp. 4947–4954, 2020.
- [15] M. Neumann and J. Burgner-Kahrs, “Considerations for follow-the-leader motion of extensible tendon-driven continuum robots,” in *2016 IEEE international conference on robotics and automation (ICRA)*. IEEE, 2016, pp. 917–923.
- [16] Y. Chen, J. Liang, and I. W. Hunter, “Modular continuum robotic endoscope design and path planning,” in *2014 IEEE International Conference on Robotics and Automation (ICRA)*. IEEE, 2014, pp. 5393–5400.
- [17] T. da Veiga, J. H. Chandler, P. Lloyd, G. Pittiglio, N. J. Wilkinson, A. K. Hoshier, R. A. Harris, and P. Valdastri, “Challenges of continuum robots in clinical context: a review,” *Progress in Biomedical Engineering*, vol. 2, no. 3, p. 032003, 2020.
- [18] O. M. Omisore, S. Han, J. Xiong, H. Li, Z. Li, and L. Wang, “A review on flexible robotic systems for minimally invasive surgery,” *IEEE Transactions on Systems, Man, and Cybernetics: Systems*, vol. 52, no. 1, pp. 631–644, 2020.
- [19] R. J. Webster III and B. A. Jones, “Design and kinematic modeling of constant curvature continuum robots: A review,” *The International Journal of Robotics Research*, vol. 29, no. 13, pp. 1661–1683, 2010.
- [20] B. T. Hachen, A. Lahlou, H. Loeb, and E. W. Hawkes, “Model predictive control for tendon-driven continuum robots using a piecewise constant curvature model,” *IEEE Robotics and Automation Letters*, vol. 7, no. 2, pp. 3034–3041, 2022.
- [21] D. Trivedi, C. D. Rahn, W. M. Kier, and L. D. Walker, “Soft robotics: Biological inspiration, state of the art, and future research,” *Applied Bionics and Biomechanics*, vol. 5, no. 3, pp. 99–117, 2008.
- [22] J. Burgner-Kahrs, C. D. Rucker, and H. Choset, “Continuum robots for medical applications: A survey,” *IEEE Transactions on Robotics*, vol. 31, no. 6, pp. 1261–1280, 2015.
- [23] B. Moradkhani, P. Kheradmand, H. Jella, J. Klein, A. Zemmar, and Y. Chitalia, “Exonav ii: Design of a robotic tool with follow-the-leader motion capability for lateral and ventral spinal cord stimulation (scs),” *arXiv preprint arXiv:2503.04603*, 2025.
- [24] D. C. Rucker and R. J. Webster III, “Statics and dynamics of continuum robots with general tendon routing and external loading,” *IEEE Transactions on Robotics*, vol. 27, no. 6, pp. 1033–1044, 2011.
- [25] Y. Wenlong, D. Wei, and D. Zhijiang, “Mechanics-based kinematic modeling of a continuum manipulator,” in *2013 IEEE/RSJ international conference on intelligent robots and systems*. IEEE, 2013, pp. 5052–5058.
- [26] P. J. Swaney, P. A. York, H. B. Gilbert, J. Burgner-Kahrs, and R. J. Webster III, “Design, fabrication, and testing of a needle-sized wrist for surgical instruments,” *Journal of medical devices*, vol. 11, no. 1, p. 014501, 2017.
- [27] P. E. Dupont, J. Lock, B. Itkowitz, and E. Butler, “Design and control of concentric-tube robots,” *IEEE Transactions on Robotics*, vol. 26, no. 2, pp. 209–225, 2010.
- [28] J. Ha, A. Mondal, Z. Zhao, A. K. Kaza, and P. E. Dupont, “Pediatric airway stent designed to facilitate mucus transport and atraumatic removal,” *IEEE Transactions on Biomedical Engineering*, vol. 67, no. 1, pp. 177–184, 2019.
- [29] Y. Chitalia, X. Wang, and J. P. Desai, “Design, modeling and control of a 2-dof robotic guidewire,” in *2018 IEEE International Conference on Robotics and Automation (ICRA)*. IEEE, 2018, pp. 32–37.
- [30] T. K. Morimoto, E. W. Hawkes, and A. M. Okamura, “Design of a compact actuation and control system for flexible medical robots,” *IEEE robotics and automation letters*, vol. 2, no. 3, pp. 1579–1585, 2017.